Power Electronics and Drives
Volume 10(45), 2025 DOI: 10.2478/pead-2025-0020

Power Electronics and Drives

A Novel Discrete Resonant Control Method for Cascaded H-Bridge Rail Balancers

Research Paper

Milos Straka*, Jaroslav Dragoun, Jakub Talla, Vojtech Blahnik, Martin Pittermann, Zdenek Peroutka

University of West Bohemia, RICE, Pilsen Czech Republic

Received: 24 July, 2025; Received in the revised form: 19 August, 2025; Accepted: 26 August, 2025

Abstract: This paper presents the concept of an advanced rail balancer (ARB) for next-generation traction substations (TSSs), along with its control algorithm based on a novel advanced resonant controller. The ARB utilises a cascaded H-bridge (CHB) converter topology and is designed to effectively address several key issues in modern TSSs, including load current symmetrisation in the distribution power grid, reactive power compensation, harmonic currents from railway vehicles and active filtering of higher-order harmonics in the grid current. The proposed asymmetric control of the ARB converter includes individual ARB phase current control using an advanced resonant controller. The resonant controller algorithm provides the desired frequency response without offset and uses direct latency compensation to mitigate the effects of low switching frequency and large control sampling times. Experimental results show very good performance of the proposed control algorithm, especially for grid current harmonics filtration with low ARB switching frequency, large sampling times and control latency.

Keywords: *active filters • cascaded H-bridge converters • current control • railway traction*

1. Introduction

Nowadays, AC railway electrification systems are becoming increasingly preferred (Steimel, 2014). The main advantage of AC infrastructure is its higher power density and its ability to integrate with smart grids under the Industry 4.0 concept through advanced traction substations (TSSs).

One of the most common approaches in newly developed railway systems is the use of an uninterrupted contact wire, which requires TSSs based on semiconductor technology.

The current state of TSS topologies can be roughly classified into two groups: those that utilise power electronics and those that do not. A comprehensive list of topology descriptions and comparisons is provided in Straka et al. (2021).

We introduce a novel solution called the advanced rail balancer (ARB), which has shown promising results. The ARB is designed for the 25 kV/50 Hz traction catenary system used in Central and Eastern Europe. Its configuration is shown in Figure 1 and includes a three-phase TSS transformer for voltage adjustment and galvanic isolation, an electronic balancer and a phase-shifting device. The core of the system is the electronic balancer, which provides full power symmetrisation. In addition to this primary function, the device also compensates for reactive power and filters high-harmonic currents. The phase-shifting device adjusts the voltage output vector to enable coordination with nearby TSSs and eliminates the need for neutral sections (voltage-free zones). Moreover, the system offers limited functionality in the event of a failure of any electronic component, which is advantageous in terms of TSS reliability and overall cost compared to TSSs using static frequency converters (SFCs). Both solutions (ARB and SFC) are described and compared in more detail in Straka et al. (2021).

* *Email: strakami@fel.zcu.cz*

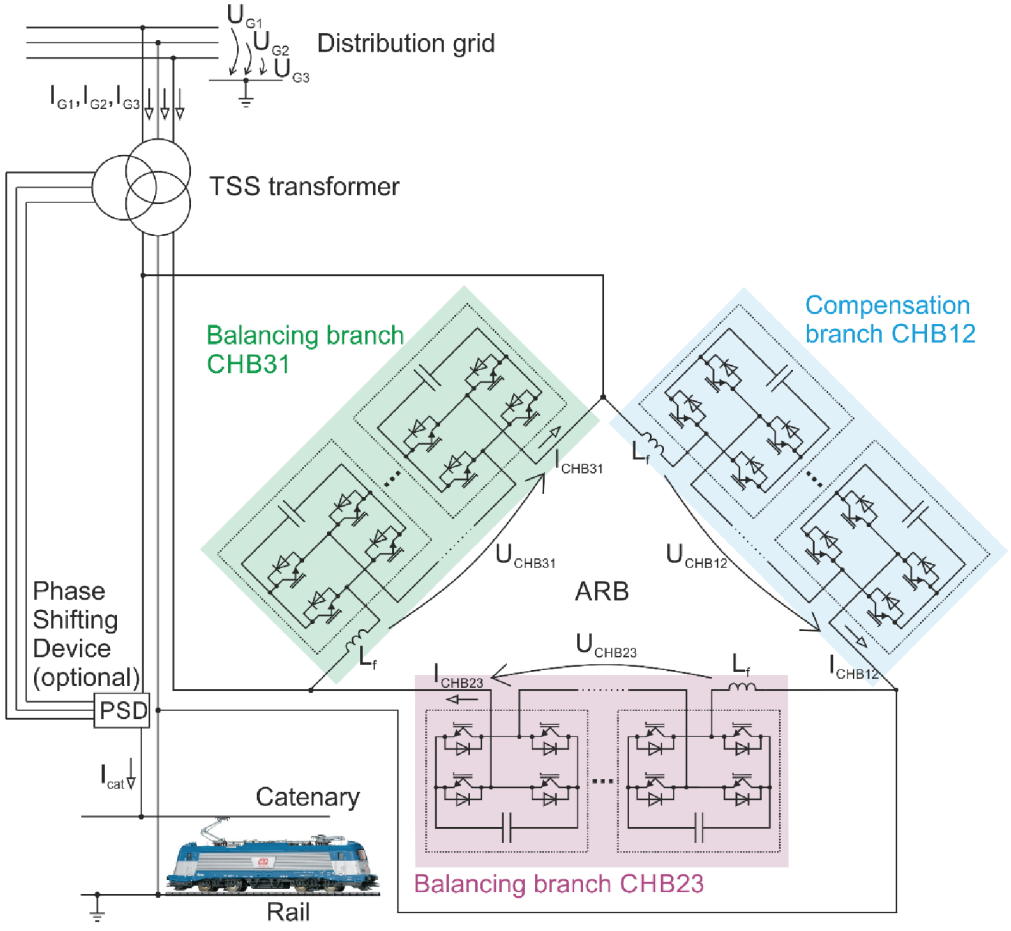

Figure 1. Topology of a TSS with the ARB. ARB, advanced rail balancer; PSD, phase shifting device; TSS, traction substation.

The presented electronic balancer unit of ARB contains a multilevel cascaded H-bridge (CHB) converter, which enhances the quality of the output voltage and supports higher operating voltage—key advantages of multilevel converters. CHB converters are widely used in applications such as active filters (Aguilera et al., 2024; Alonso Orcajo et al., 2020; Wang and Liu, 2019), photovoltaic converters (Pastor and Dudrik, 2015; Wang et al., 2019; Yu et al., 2017), static compensators (Zhang et al., 2020) or solid-state transformers (Chai, 2018).

The state-of-the-art research in the field of CHB converter control is focused mainly on single-phase systems (He et al., 2023; Ma et al., 2020; Wang et al., 2020; Zhao and Chen, 2022), modulation techniques (Alcaide et al., 2021; Lamb et al., 2018; Marquez et al., 2020), current control loops (Ma et al., 2020; Tafti et al., 2018), voltage control loops (Deng et al., 2023) and the currently popular model predictive control algorithms (Nasiri et al., 2019).

From a control perspective, the ARB functions as a shunt active power filter (SAPF), symmetrising and filtering the railway load current. The popular SAPF current control methods are variable switching frequency methods, such as direct power control (Ouchen et al., 2021), finite control set-model predictive control (FCS-MPC, Ferreira et al., 2018; Khan et al., 2020) and hysteresis current control (Abdel-Aziz et al., 2024; Chavali et al., 2022), and fixed switching frequency control methods, which are more suitable for high power applications, using synchronous reference frame control (Alonso Orcajo et al., 2020; Wang and Liu, 2019), p-q theory (Biyya et al., 2023), wavelets and adaptive filtering (Fei et al., 2023; Moradi and Pichan, 2022) methods and proportional resonant (PR) controllers (Santiprapan et al., 2024).

The presented control strategy for the CHB converter, applied in the ARB system, incorporates a power symmetrisation method based on Steinmetz's symmetrising circuit. It also includes a sliding discreet Fourier transformation (SDFT; Park, 2017) for fundamental load current harmonic estimation, dual second-order generalised integrator phase-locked loop (DSOGI-PLL) for grid synchronisation (He et al., 2018) and a novel discrete-time

state-space algorithm for PR current controllers in the ARB. This control scheme is designed with respect to the transient dynamics of the traction catenary system, while minimising undesirable effects on the distribution grid. This paper presents individual current control of ARB branches based on PR controllers, which ensures sufficiently fast and accurate per-phase current control in the stationary reference frame (with high reliability, simplicity and immunity to interference), and furthermore allows operation in the event of an ARB branch fault. However, control system latency, caused by the low switching frequency and the digital implementation of the resonant part of the PR controllers, can significantly degrade control performance or even lead to instability (Husev et al., 2020; Yepes et al., 2010). To address this, we have developed a new resonant controller algorithm with latency compensation, precise numerical implementation and orthogonal output structure, enabling sinusoidal output limiting and anti-windup protection (Lezana et al., 2007).

2. Control of ARB

In the following section, the proposed control algorithm is described in more detail. It consists of multiple parts, such as Steinmetz's equations for TSS power balancing, feedforward voltage calculation, load active and reactive power evaluation, DC-link voltage control and inner-loop current control. The DC-link voltage and current control are implemented separately for each branch, as shown in Figure 2.

2.1. Grid synchronisation

Synchronisation with the three-phase grid voltage must provide fast and accurate estimation of the voltage vector (i.e. voltage vector amplitude U_m, voltage vector angle ϑ_{u12}, and grid frequency ω). The DSOGI-PLL synchronisation

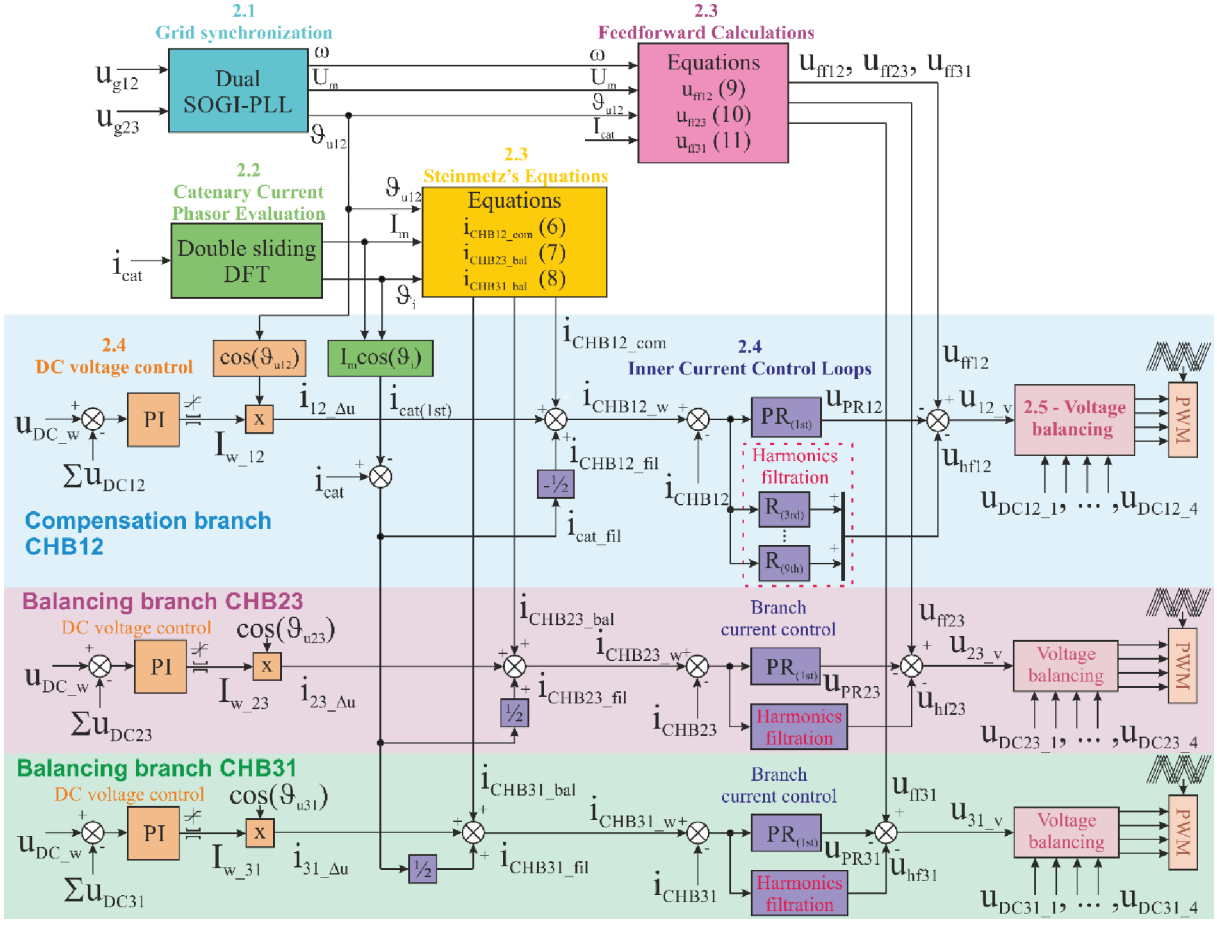

Figure 2. Block diagram of the proposed control scheme. PI, proportional integration; SOGI-PLL, second-order generalized integrator phase-locked loop.

method has been chosen for its good immunity to input signal noise and disturbances. This method is well known from Suul et al. (2012).

2.2. Catenary current phasor evaluation

To calculate the value of the compensation and symmetrisation currents accurately, it is necessary to evaluate the phasor of the single-phase current flowing through the TSS to the traction catenary $I_{cat\_SDFT\_I}$ and $I_{cat\_SDFT\_R}$. The evaluation of the current phasor is based on the following SDFT Eqs (1) and (2):

$$\begin{bmatrix} I_{cat\_SDFT\_R(k+1)} \\ I_{cat\_SDFT\_I(k+1)} \end{bmatrix} = R \begin{bmatrix} I_{cat\_SDFT\_R(k)} \\ I_{cat\_SDFT\_I(k)} \end{bmatrix} + \frac{2}{N} \begin{bmatrix} i_{cat(k)} - i_{cat(k-N)} \\ 0 \end{bmatrix} \tag{1}$$

$$R = \begin{bmatrix} \cos\left(\omega_{(k)}\Delta t\right) & -\sin\left(\omega_{(k)}\Delta t\right) \\ \sin\left(\omega_{(k)}\Delta t\right) & \cos\left(\omega_{(k)}\Delta t\right) \end{bmatrix} \tag{2}$$

where N is the length of the SDFT buffer, $\omega_{(k)}$ is the analysed frequency (~50 Hz) and Δt is the sampling period. The current amplitude and vector angle are calculated using the Eq. (3):

$$\begin{aligned} I_{cat\_m} &= \sqrt{I_{cat\_SDFT\_R(k+1)}{}^2 + I_{cat\_SDFT\_I(k+1)}{}^2} \\ \vartheta_i &= \tan^{-1}\left(\frac{I_{cat\_SDFT\_I(k+1)}}{I_{cat\_SDFT\_R(k+1)}}\right) \end{aligned} \tag{3}$$

The SDFT is a very effective and robust algorithm for spectral calculation. On the contrary, the main drawback is numerical instability. Compared to the common SDFT, we used a dual SDFT containing two independent phasor calculations using the same data. The calculated phasors are periodically reset to zero after two SDFT window length periods. However, the reset of the phasors of each SDFT is time-shifted. After resetting the first SDFT, the results of the second SDFT are used. After one window-length period following the first SDFT reset, the first SDFT converges to the correct value, its result can then be used, and the second SDFT can be reset, and vice versa. A detailed description of this algorithm and implementation information can be found in Talla and Blahnik (2017).

2.3. Steinmetz's equations and voltage feedforward calculation

Defining symmetrisation and reactive power compensation of a single-phase load connected to the TSS catenary is based on Steinmetz's equivalent circuit and explained by a phasor diagram in Figure 3. The balancing current calculation depends on the catenary current amplitude and its phase shift relative to the grid voltage [Eqs (4) and (5)]. Eqs (6)–(8) describe ARB reactive power compensating and balancing currents of individual CHB branches based on the catenary current. The I_{cat_m} is the catenary current magnitude, ϑ_{u12} is the voltage vector angle (line to line U_{g12} voltage angle) and ϑ_i is the current vector angle of the catenary load. The calculated currents i_{CHB12}, i_{CHB23} and i_{CHB31} are used as a fundamental harmonic current reference for the ARB inner current loop.

$$I_{cat\_I} = I_{cat\_m} \sin\left(\vartheta_{u12} - \vartheta_i\right) \tag{4}$$

$$I_{cat\_R} = I_{cat\_m} \cos\left(\vartheta_{u12} - \vartheta_i\right) \tag{5}$$

$$i_{CHB12\_com} = I_{cat\_I} \cos\left(\vartheta_{u12} + \frac{\pi}{2}\right) \tag{6}$$

$$i_{CHB23\_bal} = I_{cat\_R}\left(\frac{1}{\sqrt{3}}\cos\left(\vartheta_{u12} - \frac{5\pi}{6}\right) + \cos\left(\vartheta_{u12}\right)\right) = \frac{I_{cat\_R}}{\sqrt{3}}\cos\left(\vartheta_{u12} - \frac{\pi}{6}\right) \tag{7}$$

$$i_{CHB31\_bal} = I_{cat\_R}\left(-\frac{1}{\sqrt{3}}\cos\left(\vartheta_{u12} - \frac{\pi}{6}\right) + \cos\left(\vartheta_{u12}\right)\right) = \frac{I_{cat\_R}}{\sqrt{3}}\cos\left(\vartheta_{u12} + \frac{\pi}{6}\right) \tag{8}$$

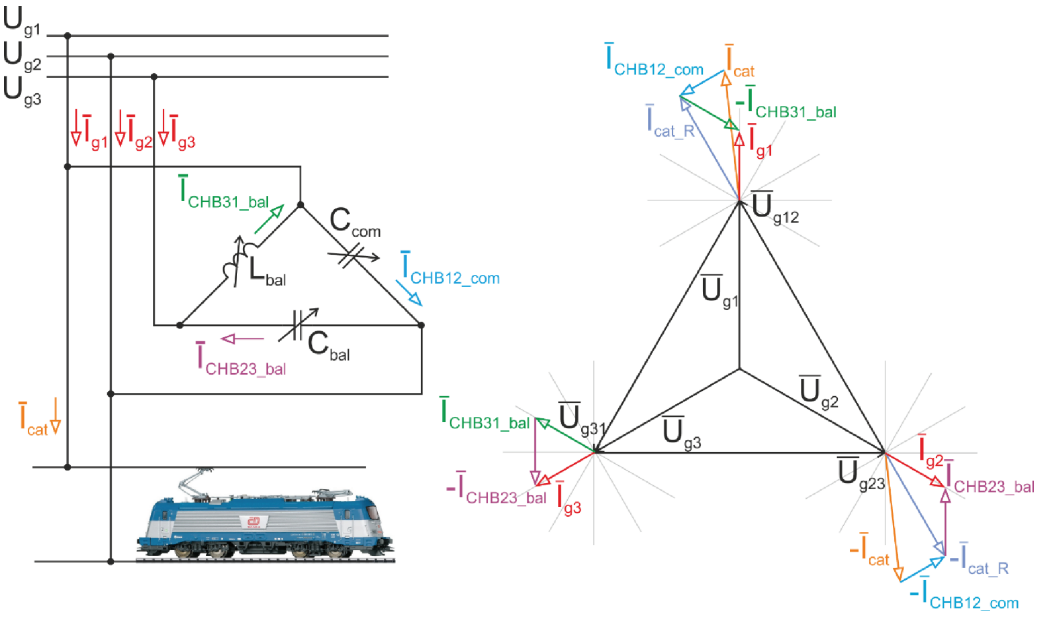

Figure 3. Steinmetz's symmetrising circuit and corresponding phasor diagram illustrating the function of the electronic balancer.

The feedforward calculation is based on a simplified electrical steady-state model of the device: a series connection of the grid voltage, filter inductance L_{CHB} with the effect of filter resistance neglected and converter voltage. The resulting feedforward converter voltages u_{ff12}, u_{ff23}, u_{ff31}, depending on the grid voltage U_m, ϑ_{u12}, frequency ω and catenary current I_{cat_I}, I_{cat_R} are presented in Eqs (9)–(11). The filter inductance voltage drop is shifted by $-\pi/2$ to CHB currents as presented by Eqs (6)–(8).

$$u_{ff12} = U_m \cos\left(\vartheta_{u12}\right) + \omega L_f I_{cat\_I} \cos\left(\vartheta_{u12}\right) \tag{9}$$

$$u_{ff23} = U_m \cos\left(\vartheta_{u12} - \frac{2\pi}{3}\right) + \frac{\omega L_f I_{cat\_R}}{\sqrt{3}} \cos\left(\vartheta_{u12} - \frac{2\pi}{3}\right) \tag{10}$$

$$u_{ff31} = U_m \cos\left(\vartheta_{u12} + \frac{2\pi}{3}\right) + \frac{\omega L_f I_{cat\_R}}{\sqrt{3}} \cos\left(\vartheta_{u12} - \frac{\pi}{3}\right) \tag{11}$$

2.4. DC-link voltage and inner current control loops

The DC-link voltages and CHB currents of each ARB branch are controlled individually. The DC-link voltage control provides an approximately constant sum of DC-link voltages of floating capacitors of all cascaded-connected H-bridges per CHB phase (u_{DC_w} is the total reference voltage of the whole CHB branch). The DC-link capacitor's energy covers the power losses of the converter and the fluctuation of reactive power. Since the power losses are low, fast dynamics of the DC-link voltage controller are not required. Therefore, a proportional integral (PI) voltage controller with a dominant integral component was chosen. The output signal of the voltage controller is the required current $I_{12\_\Delta u}$, which is in phase with the grid voltage (active current). This current is summed with the required symmetrising current from Steinmetz's Eqs (6)–(8), and with the required higher-order harmonics filtration current i_{CHB12_fil}. This creates the total reference current of the CHB branch i_{CHB12_w}.

The required catenary filtration current i_{cat_fil} is calculated as the difference between the actual catenary current i_{cat} and the fundamental harmonic of the catenary current $i_{cat(1st)}$ estimated by SDFT. The required filtration current is equally divided into two parallel branches: (1) compensation branch CHB12 $i_{CHB12\_fil} = -1/2\ i_{cat\_fil}$ and (2) the entire symmetrisation branch, consisting of a series connection of CHB23 and CHB31 branches $i_{CHB23\_fil} = i_{CHB31\_fil} = 1/2\ i_{cat\_fil}$. However, the harmonic current distribution in parallel branches can be freely selected, for example, with respect to branch power losses.

The total current reference i_{CHB12_w} is used as a reference for a proportional controller and several advanced PR controllers regulating the fundamental harmonic component (50 Hz) and higher-order harmonics (150 Hz, 250 Hz, 350 Hz and 450 Hz). The PR controller generates a signal u_{PR12}, which is summed in the following step with a feedforward value, u_{ff12} Eq. (9), and a harmonics filtration component, also denoted as u_{hf12}. The result is the converter modulation signal for the CHB 1 kHz phase shift pulse width modulation (PS-PWM) modulator, including the DC-link balancing algorithm. Low switching and sampling frequency, large control latency, and the requirement to eliminate higher-order current harmonics up to 450 Hz are the biggest challenges in ARB control, which led to the development of the advanced R controller algorithm presented in Section 3.

2.5. PS-PWM modulation and individual H-bridge voltage balancing

In the given application, a multilevel voltage source inverter (VSI) is used in combination with PS-PWM. To better understand the delays introduced into the system, see Figure 4. The base sampling frequency of the system is 8 kHz (sampling is at the top and bottom of all phase-shifted PWM timers). However, the compare register of each H-bridge is only changed at its top or bottom of the PWM timer (two times per PWM frequency, i.e. 2 kHz). It creates the variable control delay of individual inverters.

This means that, at a given instant, it takes 1 sample time for the measured values to be processed and set as the active output voltage reference for the first converter, 2 sample times for second converter up to 4 sample times for the fourth converter. This reference remains active for a duration of four samples before being replaced by a new value.

The latency in the system that needs to be compensated corresponds to one sample delay due to computation, plus half of the time during which the reference value is active. In this case, the total compensated delay is equivalent to three sampling steps. This value is primarily influenced by the number of levels in the multilevel VSI used.

To model the real PS-PWM latency and demonstrate its effect, discrete state-space equations have been derived for the PS-PWM:

$$\begin{bmatrix} u_{CHB\_X.1(k)} \\ u_{CHB\_X.2(k)} \\ u_{CHB\_X.3(k)} \\ u_{CHB\_X.4(k)} \end{bmatrix} = \begin{bmatrix} 0 & 0 & 0 & 0 \\ 1 & 0 & 0 & 0 \\ 0 & 1 & 0 & 0 \\ 0 & 0 & 1 & 0 \end{bmatrix} \begin{bmatrix} u_{CHB\_X.1(k-1)} \\ u_{CHB\_X.2(k-1)} \\ u_{CHB\_X.3(k-1)} \\ u_{CHB\_X.4(k-1)} \end{bmatrix} + \begin{bmatrix} 1 \\ 0 \\ 0 \\ 0 \end{bmatrix} u_{CHB\_X(k)} \tag{12}$$

A method for balancing individual cells of CHB based on energy formula at the modulation signal level was used (Blahnik et al., 2018). The PS-PWM is modulator implemented in an Altera/Intel Cyclone III, FPGA.

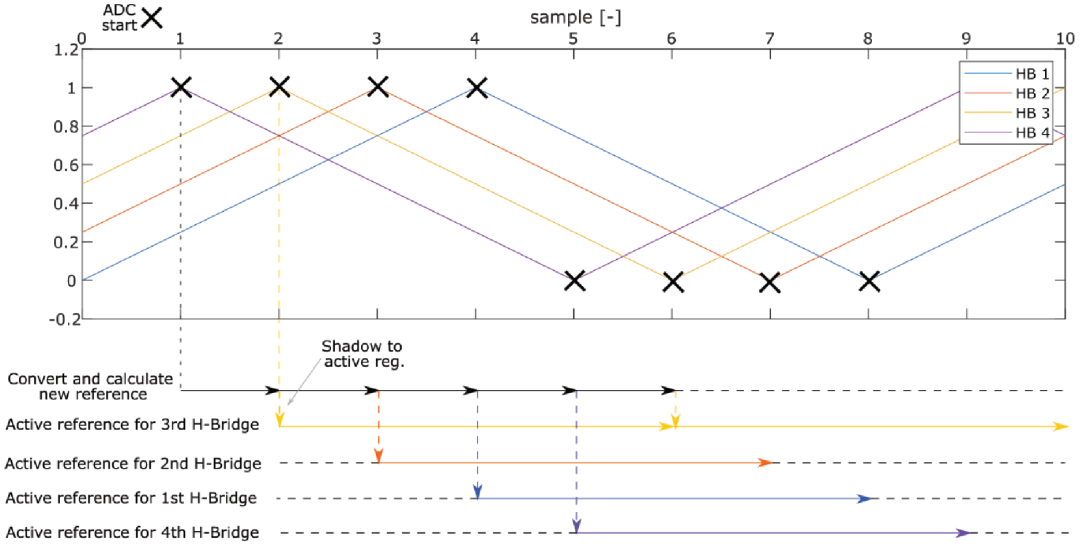

Figure 4. Timeline visualising control and modulation delay of the system.

3. Advanced resonant controller algorithm

This section describes a new R controller algorithm for control of ARB currents fundamental and higher order harmonics with improved numerical properties based on analytical exact discretisation and control latency compensation. The implementation of the R controller has a significant impact on control quality, especially with large sample times or control latencies (Husev et al., 2020). In contrast to the PI controller, the PR controller can directly regulate AC signals without steady-state errors. The PR controller consists of a proportional part and a resonant part:

$$F_{PR(s)} = K_P + F_{REZ(s)} = K_P + K_R \frac{\omega s}{s^2 + \omega^2} \tag{13}$$

where KP is the proportional gain, KR is a resonant gain and ω is the resonant angular frequency.

3.1. State space form of resonant controller

The digital implementation of the R controller can be derived by transforming the transfer function (13) into a Laplace equation:

$$y_{(s)} = \frac{1}{s}\left(K_R \omega u_{(s)} - \omega^2 \frac{1}{s} y_{(s)} \right) \tag{14}$$

Eq. (14) can be reformulated into a state-space equation using the general formula:

$$\begin{aligned} sx &= Ax + Bu \\ y &= Cx + Du \end{aligned} \tag{15}$$

From Eqs (14) and (15), we can obtain the state-space equations of the R controller:

$$s\begin{bmatrix} x_\alpha \\ x_\beta \end{bmatrix} = \begin{bmatrix} 0 & -\omega \\ \omega & 0 \end{bmatrix}\begin{bmatrix} x_\alpha \\ x_\beta \end{bmatrix} + \begin{bmatrix} K_R\omega \\ 0 \end{bmatrix} u$$

$$y = \begin{bmatrix} 1 & 0 \end{bmatrix}\begin{bmatrix} x_\alpha \\ x_\beta \end{bmatrix} \tag{16}$$

where $x_\alpha = y$ is the R controller output and $x_\beta = \frac{1}{s}\omega x_\alpha = \frac{1}{s}\omega y$ creates orthogonal (imaginary complement) part of the R controller output.

3.2. Discrete state space form of resonant controller

The matrix A can be expressed as follows:

$$A = \begin{bmatrix} 0 & -\omega \\ \omega & 0 \end{bmatrix} = j\omega \begin{bmatrix} 0 & j \\ -j & 0 \end{bmatrix} \tag{17}$$

where *j* is imaginary operator.

By using the exact discretisation formula for matrix A and sampling time Δt,

$$A_d = e^{A\Delta t} = e^{j\omega\Delta t\begin{bmatrix} 0 & j \\ -j & 0 \end{bmatrix}} \tag{18}$$

We get the following analytical solution:

$$A_d = \begin{bmatrix} \cos(\omega\Delta t) & -\sin(\omega\Delta t) \\ \sin(\omega\Delta t) & \cos(\omega\Delta t) \end{bmatrix} \tag{19}$$

The result is an orthonormal (rotational) matrix ($A_d^{-1} = A_d^T$).
We can use the exact discretisation formula for the B matrix:

$$B_d = A^{-1}\left(A_d - I\right)B \tag{20}$$

So:

$$B_d = \frac{1}{\omega}\begin{bmatrix} 0 & 1 \\ -1 & 0 \end{bmatrix}\begin{bmatrix} \cos(\omega\Delta t)-1 & -\sin(\omega\Delta t) \\ \sin(\omega\Delta t) & \cos(\omega\Delta t)-1 \end{bmatrix}\begin{bmatrix} K_R\omega \\ 0 \end{bmatrix} = K_R\begin{bmatrix} \sin(\omega\Delta t) \\ 1-\cos(\omega\Delta t) \end{bmatrix} \tag{21}$$

Resulted R controller equations are:

$$\begin{bmatrix} x_{\alpha(k)} \\ x_{\beta(k)} \end{bmatrix} = \begin{bmatrix} \cos(\omega\Delta t) & -\sin(\omega\Delta t) \\ \sin(\omega\Delta t) & \cos(\omega\Delta t) \end{bmatrix}\begin{bmatrix} x_{\alpha(k-1)} \\ x_{\beta(k-1)} \end{bmatrix} + K_R\begin{bmatrix} \sin(\omega\Delta t) \\ 1-\cos(\omega\Delta t) \end{bmatrix}u_{(k)}$$

$$y_{(k)} = \begin{bmatrix} 1 & 0 \end{bmatrix}\begin{bmatrix} x_{\alpha(k)} \\ x_{\beta(k)} \end{bmatrix} = x_{\alpha(k)} \tag{22}$$

where $u_{(k)} = e_{(k)}$ is the difference between required and actual/measured value and $y_{(k)}$ is the R controller output. If $\omega\Delta t \cong 0$ then:

$$A_d \cong \begin{bmatrix} 1 & -\omega\Delta t \\ \omega\Delta t & 1 \end{bmatrix}, \quad B_d \cong K_R\begin{bmatrix} \omega\Delta t \\ 0 \end{bmatrix} \tag{23}$$

leads to the forward Euler discretisation of the R controller Eq. (23).

3.3. Latency compensation of resonant controller

The control algorithm's latency can reduce the efficiency of the R or even make it unstable. However, the R controller in the state-space form can be easily extended with feedforward latency compensation included in the C matrix. The original output matrix contains only the selection operation of the first state ($x_{\alpha(k)}$). If we define the control latency as Δt_{lat}, we can calculate feedforward latency compensation by multiplying the original C matrix by orthogonal rotational matrix as:

$$y_{(k)} = \begin{bmatrix} 1 & 0 \end{bmatrix}\begin{bmatrix} \cos(\omega\Delta t_{lat}) & -\sin(\omega\Delta t_{lat}) \\ \sin(\omega\Delta t_{lat}) & \cos(\omega\Delta t_{lat}) \end{bmatrix}\begin{bmatrix} x_{\alpha(k)} \\ x_{\beta(k)} \end{bmatrix} = \begin{bmatrix} \cos(\omega\Delta t_{lat}) & -\sin(\omega\Delta t_{lat}) \end{bmatrix}\begin{bmatrix} x_{\alpha(k)} \\ x_{\beta(k)} \end{bmatrix} \tag{24}$$

The matrix rotates the R controller outputs by an angle equivalent to the time latency multiplied by the angular velocity of the R controller. The resulting C matrix is shown in the Eq. (24).

To completely eliminate latency effect on R controller, the direct link between control error and the controller output (D matrix in state space model) behaving like a proportional controller can be calculated according to Eq. (25). This component can usually be neglected when PR controller is used due to the low impact to the complete proportional gain.

$$y_{(k)} = \begin{bmatrix} \cos(\omega\Delta t_{lat}) & -\sin(\omega\Delta t_{lat}) \end{bmatrix}\begin{bmatrix} x_{\alpha(k)} \\ x_{\beta(k)} \end{bmatrix} + K_R\sin(\omega\Delta t_{lat})u_{(k)} \tag{25}$$

The complete equations with latency compensation of advanced PR controller are:

$$\begin{bmatrix} x_{\alpha(k)} \\ x_{\beta(k)} \end{bmatrix} = \begin{bmatrix} \cos(\omega\Delta t) & -\sin(\omega\Delta t) \\ \sin(\omega\Delta t) & \cos(\omega\Delta t) \end{bmatrix}\begin{bmatrix} x_{\alpha(k-1)} \\ x_{\beta(k-1)} \end{bmatrix} + K_R\begin{bmatrix} \sin(\omega\Delta t) \\ 1-\cos(\omega\Delta t) \end{bmatrix}u_{(k)}$$

$$y_{(k)} = \begin{bmatrix} \cos(\omega\Delta t_{lat}) & -\sin(\omega\Delta t_{lat}) \end{bmatrix}\begin{bmatrix} x_{\alpha(k)} \\ x_{\beta(k)} \end{bmatrix} + \left(K_P + K_R\sin(\omega\Delta t_{lat})\right)u_{(k)}, \tag{26}$$

where $u_{(k)} = e_{(k)}$ is the difference between required and actual/measured value and $y_{(k)}$ is the PR controller output.

3.4. Advanced resonant controller evaluation

For comparison purposes, three implementation alternatives were selected: the Basic R controller Eqs (27) and (29) as an effective common R implementation, the R controller based on Tustin discretisation (Yepes et al., 2010) Eq. (30), and the first-order hold (FOH) discretisation (Yepes et al., 2010) Eq. (31).

The Basic R controller implementation is based on modification of forward Euler discretisation Eqs (27) and (28):

$$y_{(k)} = y_{(k-1)} + \left(K_R \omega u_{(k)} - \omega x_{\beta(k-1)}\right)\Delta t \tag{27}$$

$$x_{\beta(k)} = x_{\beta(k-1)} + \omega y_{(k-1)}\Delta t\,, \tag{28}$$

where $u_{(k)} = e_{(k)}$ is the difference between the required and the actual/measured value, $y_{(k)}$ is the R controller output. Using pure forward Euler discretisation, the sampling frequency of the PR controller discretised by Euler method must be around 1,000 times higher, than its resonant frequency to function properly (Yepes et al., 2010). Furthermore, the forward Euler implementation shifts the R resonant frequency. A basic and straightforward improvement of the forward Euler algorithm applies the result of the output Eq. (27) directly to update the second Eq. (28) resulting in Eq. (29):

$$x_{\beta(k)} = x_{\beta(k-1)} + \omega y_{(k)}\Delta t \tag{29}$$

A similar result can be achieved when the Eq. (29) is calculated first and its result $x_{\beta(k)}$ is immediately used for the calculation of the R output $y_{(k)}$ Eq. (27) instead of $x_{\beta(k-1)}$. This Basic algorithm of the R controller is computationally very effective (especially with variable frequency), suitable for many applications and works with a lower sampling frequency compared to forward Euler. However, for a high-power converter with low switching frequency (i.e. low sampling frequency and large control delays) which contains R controllers for higher harmonics, this R controller implementation is still insufficient and even unstable. This fact is demonstrated in later section see Figure 14.

The Tustin and FOH R controller implementations are in Eqs (30) and (31), respectively. Both the Basic and the Tustin discretisation methods shift the resonant frequency, each in the opposite direction (Figure 5). In contrast, the proposed advanced R and the FOH R controllers yield identical results, which perfectly match the ideal R controller characteristics.

$$R_{tustin(z)} = 2\Delta t \frac{1 - z^{-2}}{(\omega^2\Delta t^2 + 4) + z^{-1}\left(2\omega^2\Delta t^2 - 8\right) + z^{-2}(\omega^2\Delta t^2 + 4)} \tag{30}$$

$$R_{FOH(z)} = \frac{\left(1 - \cos(\omega\Delta t)\right)\left(1 - z^{-2}\right)}{\omega^2\Delta t\left(1 - 2z^{-1}\cos(\omega\Delta t) + z^{-2}\right)} \tag{31}$$

The influence of the control latency on the R control part of the system in the frequency domain is shown in Figure 6. The figure illustrates the effect of delay introduced by both the computation and the modulator (see Section 2.5). This delay causes a significant phase shift of uncompensated R controllers. The uncompensated R controller shown in the figure uses the FOH discretisation method. The similar results would be obtained with an uncompensated advanced R controller. The ideal frequency characteristic, used as a reference, corresponds to a continuous-time R controller without latency. The advanced R controller with delay compensation closely follows the ideal curve up to the resonant frequency, exhibiting only a small, negligible phase error at heavily damped frequencies.

The main advantage of the proposed controller over FOH lies in its simple implementation and effective control latency compensation. Furthermore, decomposition of the R controller output into two orthogonal (complex) components [x_α, x_β] allows determination of amplitude $\left(\sqrt{x_\alpha{}^2 + x_\beta{}^2}\right)$ and phase $\tan^{-1}\left(\frac{x_\alpha}{x_\beta}\right)$ of the R controller output. This information can be used for anti-windup correction, feedforward computations and other control enhancements.

On the contrary, the computational effort required by the advanced R controller compared to the forward Euler or its Basic modification involves four additional operations (multiplications or additions) and three more operations for delay compensation with constant resonant frequency (constant R coefficients).

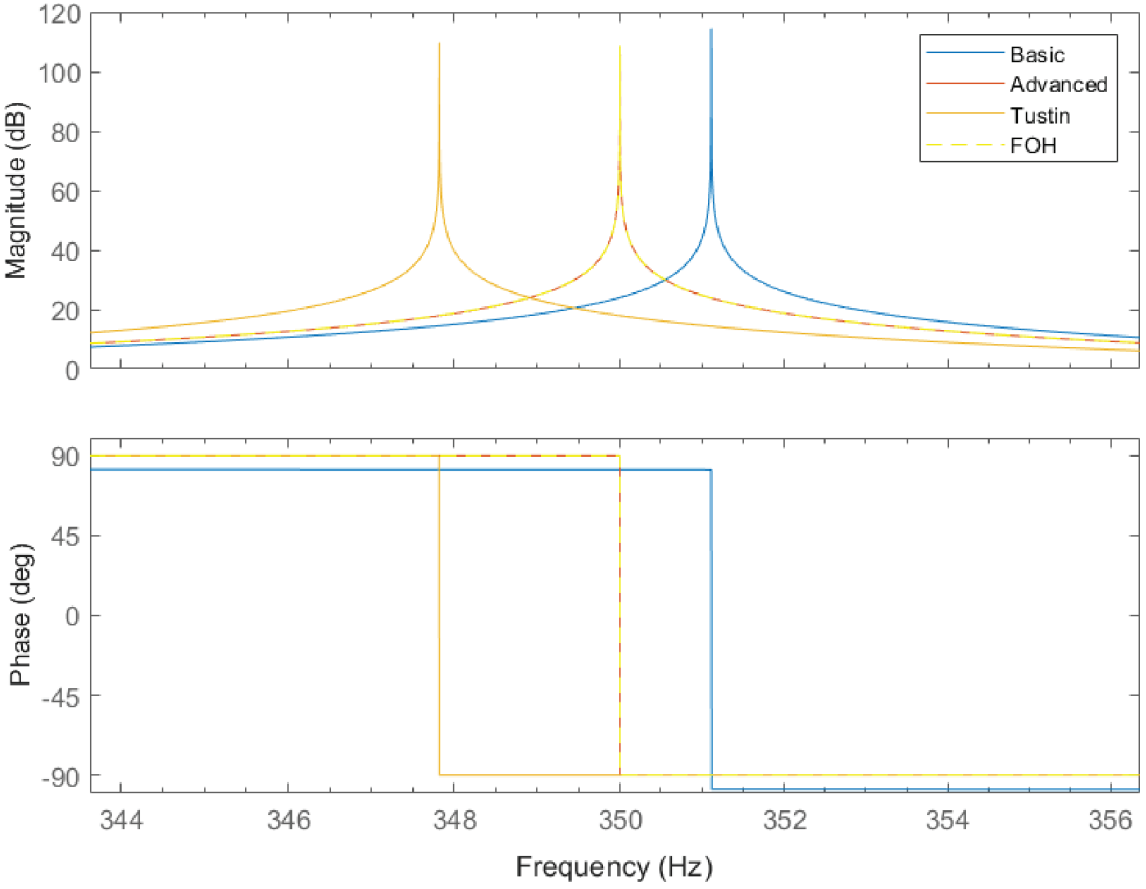

Figure 5. Influence of different discretisation techniques on R controller Bode's characteristics. FOH, first-order hold.

4. Experimental Results

The schematic diagram of the laboratory prototype (see Figure 7) corresponds to the one shown in Figure 1, except the missing phase shifting device (PSD). All of the measured values, used for control, are marked in red. The system parameters are listed in Table 1. To verify the proposed control algorithm, a down-scaled laboratory model of the ARB was built (see photo in Figure 8). Each branch of the balancer unit contains four CHBs, each equipped with a series inductor L_{CHB}. All control algorithms are executed on a Texas Instruments TMS320F28335 microcontroller. The PS-PWM is implemented in an Altera/Intel Cyclone III FPGA, which forms part of the multi-level converter (MLC) interface controller. The PS-PWM algorithm uses two self-inverted sinusoidal reference signals, one for each half of the H-bridge. Each bridge is modulated using its own carrier signal, phase-shifted by $\pi/4$ relative to the others. Interrupt handling and analog-to-digital conversion ADC are synchronised with the rising and falling edges of the 1 kHz carrier waveform.

The load of the TSS is represented as: (A) a pure RL load (Figures 9–14) or (B) a single-phase diode bridge rectifier with RL load (Figures 15–17). The load was dimensioned to comply with the limitations of the laboratory stand's circuit breaker and to match the impedance scaling requirements.

The quality of ARB control is quantitatively evaluated using the total harmonic distortion (THD), defined in Eq. (32), and by symmetrical component analysis of all grid current and voltage waveforms.

$$THD = \frac{\sqrt{\sum_{n=2}^{40} A_{m(n)}^{\ 2}}}{A_{m(1)}} \cdot 100[\%] \tag{32}$$

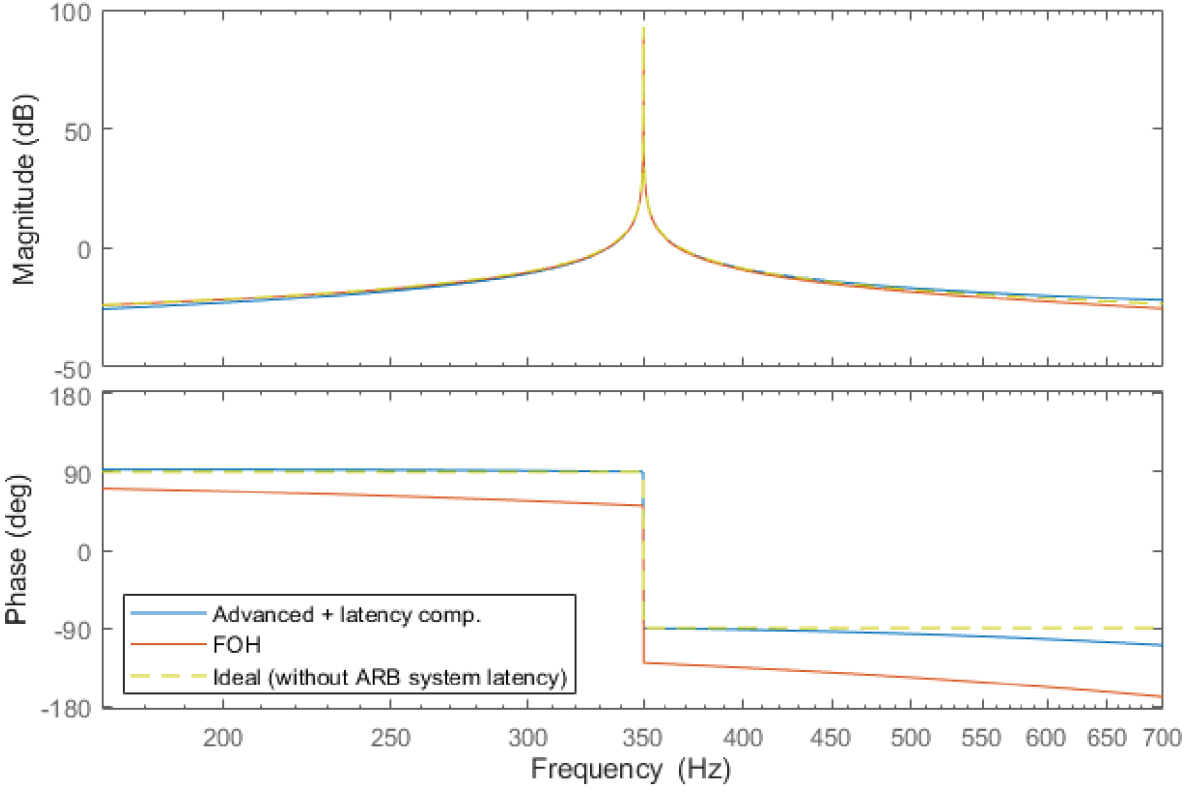

Figure 6. Bode's characteristics of discrete R controllers with ARB control system latency and ideal characteristic of continuous R controller without latency. ARB, advanced rail balancer; FOH, first-order hold.

The positive and negative sequence components of the input current waveform are calculated using the Fortescue transformation. The negative sequence is then expressed as a percentage of the positive sequence.

4.1. AC RL load

The AC RL load ($P_{(1)}$ = 8.66 kW, $Q_{(1)}$ = 3.4 kVAr) is used for testing. Figure 9 shows the operation of the TSS without ARB functionality. In this case, the catenary current I_{cat} equals the grid current I_{g1}, while $I_{g2} = -I_{g1}$ and I_{g3} = 0 A. This configuration results in the negative sequence component being 100% of the positive sequence component. The grid current is unbalanced and phase-shifted—I_{g1} leads the grid phase voltage U_{g1}, by 8.5°, indicating a capacitive character relative to the grid voltage, in contrast to the expected inductive character with respect to the catenary voltage U_{g12}.

Figure 10 shows the same RL load, but with ARB balancing enabled, excluding harmonic current filtration. While the catenary current I_{cat} remains unchanged, the amplitude and phase shift of I_{g1} relative to U_{g1} are reduced. However, significant harmonic distortion remains in the grid current, primarily caused by the ARB itself, particularly due to dead times and voltage drops across the IGBTs.

Figure 11 displays the internal ARB symmetrising currents I_{CHB} without harmonics filtration, along with the 9-level output voltage U_{CHB12} of the corresponding ARB branch during the symmetrisation process. The resulting grid currents are presented in Figure 12. The currents are successfully symmetrised, and the negative sequence component is reduced to 1.15%. Nevertheless, the grid currents still contain prominent odd-order harmonics (3rd, 5th, 7th and 9th).

Figure 13 illustrates the performance of a conventional R controller implemented using the basic discretisation method as shown in Eqs (27) and (29), and higher-order harmonics filtration. This controller exhibits divergent behaviour, especially at higher resonant frequencies, due to the ARB's control delay, large sampling time and low switching frequency. It is caused by a large basic R numerical error and uncompensated control delay (see Section 3.4).

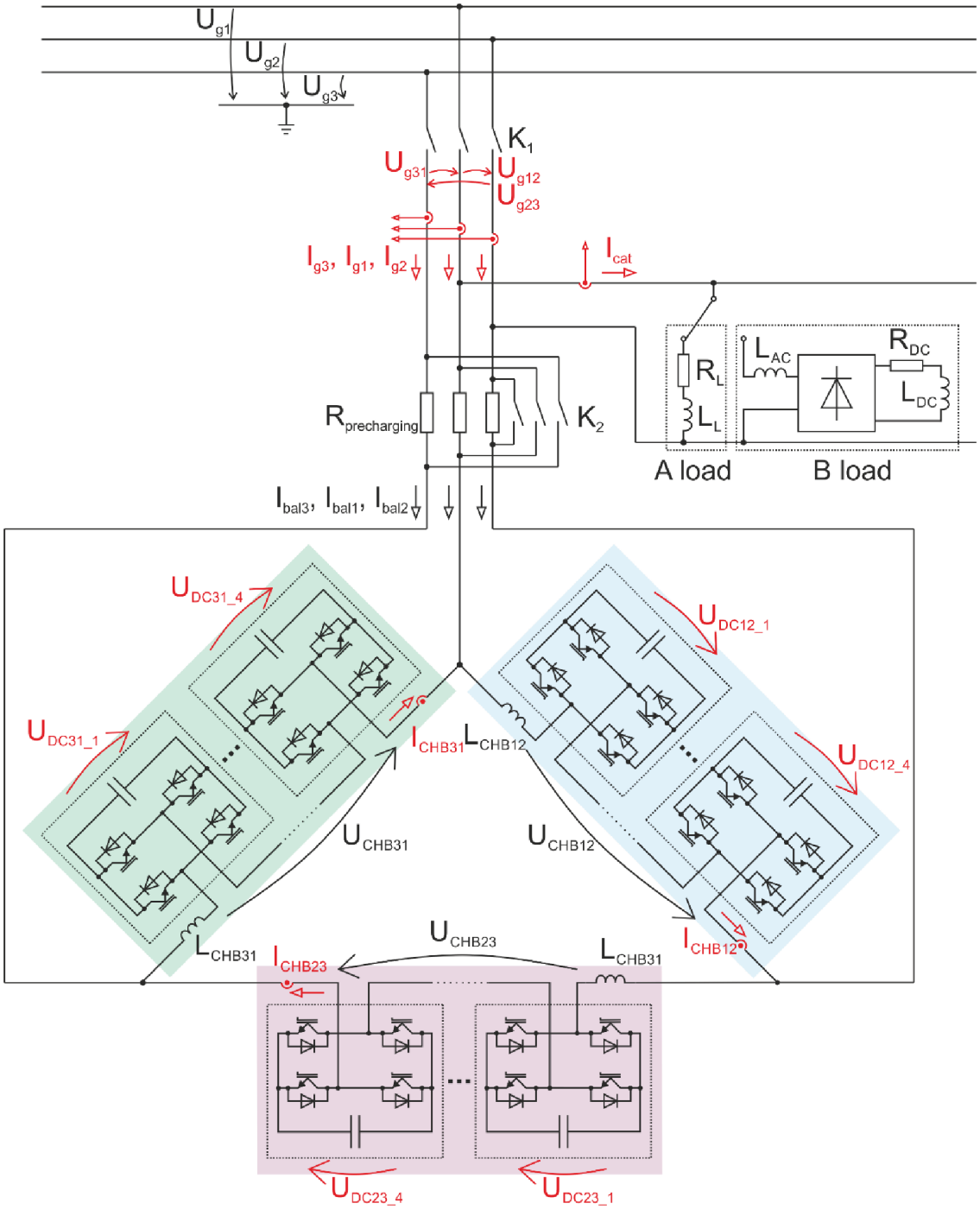

Figure 7. Scheme of the laboratory model of ARB. ARB, advanced rail balancer.

In contrast, the control employing the proposed advanced R controller with delay compensation demonstrates great performance even in harmonic current filtration, as shown in Figure 14.

4.2. Diode bridge rectifier with RL load

The diode bridge rectifier with an RL load ($P_{(1)}$ = 6.7 kW, $Q_{(1)}$ = 4.3 kVAr) is used to simulate a non-linear and unbalanced load (similar to older types of locomotives). Figure 15 shows the operation of the TSS without ARB

Table 1. Parameters of the experimental model.

Parameter	Description	Value
U_{g12}, U_{g23}, U_{g31}	Line-line voltage	400 V_{RMS}/50 Hz
L_{CHB}	Filtration inductor	4 mH
C_{CHB}	DC-link capacitor	2.5 mF
U_{DC}	DC-link voltage	180 V
ΣU_{DC}	DC-link voltage summation	4 × 180 V = 720 V
f_{PWM}	PWM frequency	1 kHz
t_{dt}	Dead time duration	1 μs
PI: K_P; T_I	PI gain and time constant	0.04, 0.2 s
$PR_{(1)}$: K_P; K_R	PR gain and time constant	2; 200
A load	RL load parameters	16 Ω, 20 mH ($P_{(1)}$ = 8.66 kW, $Q_{(1)}$ = 3.4 kVAr)
B load	Diode rectifier load parameters	AC: 10 mH; DC: 16 Ω, 80 mH ($P_{(1)}$ = 6.7 kW, $Q_{(1)}$ = 4.3 kVAr)

PI, proportional integration; PR, proportional resonation; PWM, pulse width modulation.

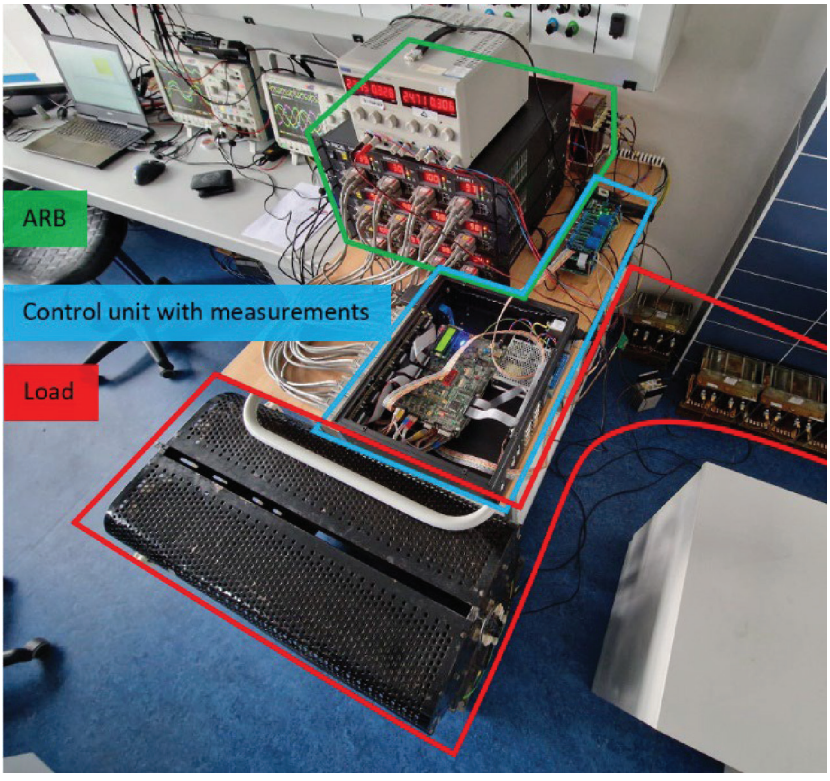

Figure 8. Laboratory prototype for experimental validation.

functionality. In this case, the catenary current I_{cat} equals the grid current I_{g1}, current $I_{g2} = -I_{g1}$ and I_{g3} = 0 A. The load introduces significant harmonic distortion, causes a phase shift and results in unbalanced current distribution.

Figure 16 presents the internal ARB (CHB) branch currents during operation with both balancing and harmonics filtration active. Approximately 50% of the harmonic content of the load current is filtered by the CHB12 branch (I_{CHB12}), and the remaining 50% is handled by the CHB23 and CHB31 branches (I_{CHB23}, I_{CHB31}).

The final grid currents are shown in Figure 17. The currents are balanced and exhibit no phase shift relative to the respective grid phase voltages, with no significant harmonic distortion. Minor current spikes are visible during diode rectifier commutation events, affecting only I_{g1} and I_{g2}, which is typical for this type of load. The further current spike reduction is limited by the Gibbs phenomenon together with the maximum order of harmonic filtration (up to 9th), which is constrained by the switching frequency of the converter, sampling frequency, DC-link voltage and size of filtering inductance.

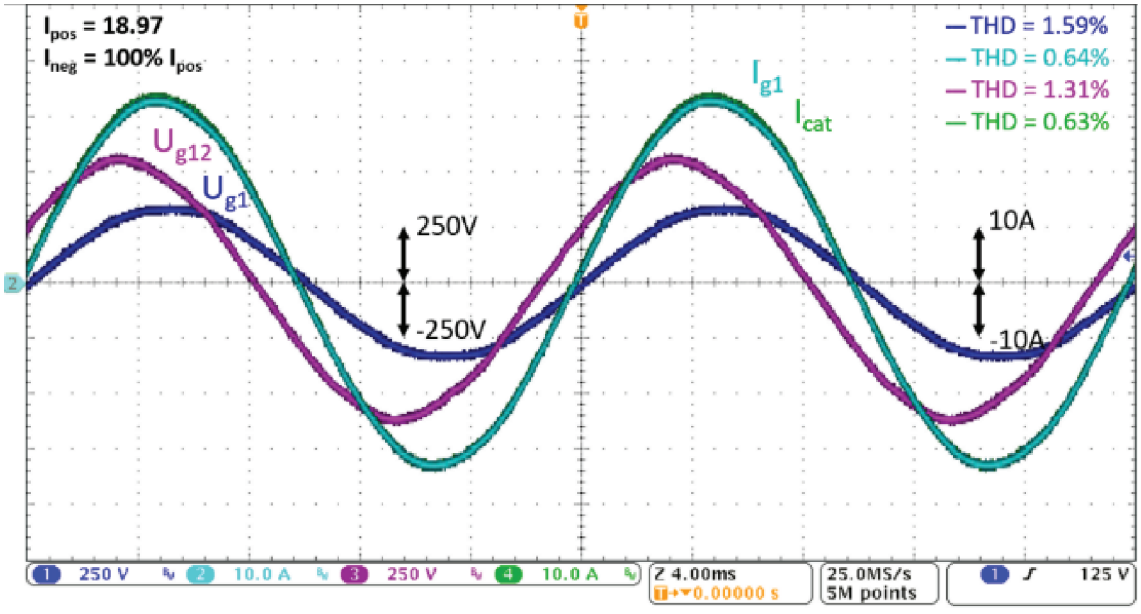

Figure 9. RL load, ARB off, blue U_{g1} [250 V/div], cyan I_{g1} [10 A/div], purple U_{g12} [250 V/div], green I_{cat} [10 A/div] (aligned with I_{g1}). ARB, advanced rail balancer; THD, total harmonic distortion.

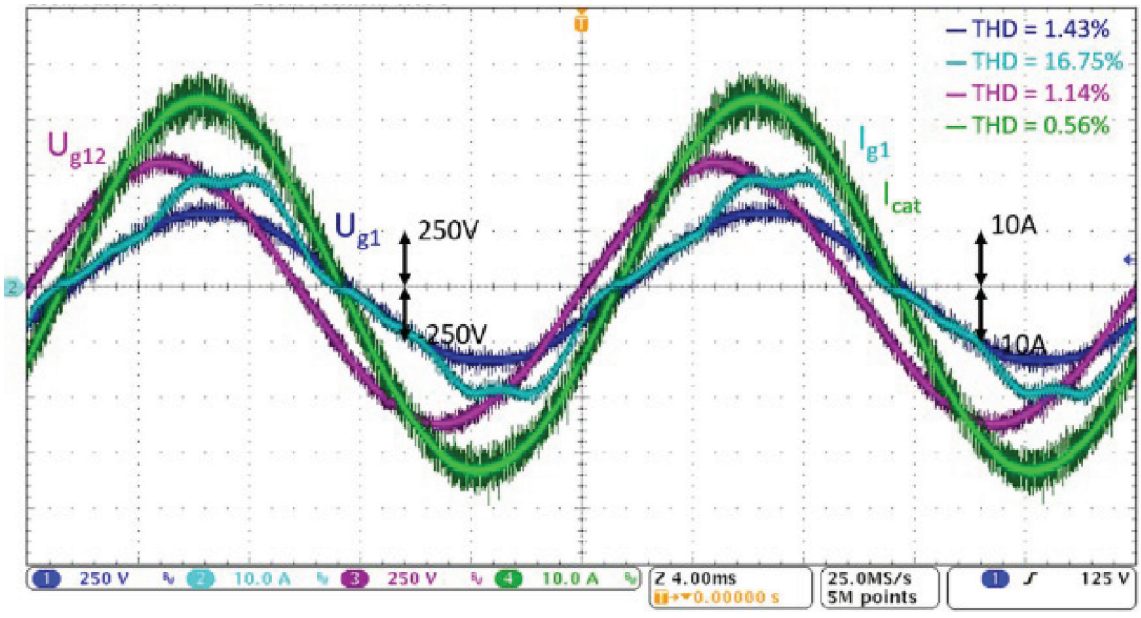

Figure 10. RL load, ARB—balancing ON + harmonics filtration OFF, blue U_{g1} [250 V/div], cyan I_{g1} [10 A/div], purple U_{g12} [250 V/div], green I_{cat} [10A/div]. ARB, advanced rail balancer; THD, total harmonic distortion.

5. Conclusion

This paper presents the ARB designed for next-generation TSSs, including its control algorithm based on a novel advanced resonant controller. The proposed ARB, based on a CHB converter topology, is validated experimentally as presented in this paper. The presented ARB solution addresses multiple challenges:

- Symmetrisation of the load current supplied from the distribution power grid.
- Compensation of reactive power generated by railway vehicles.

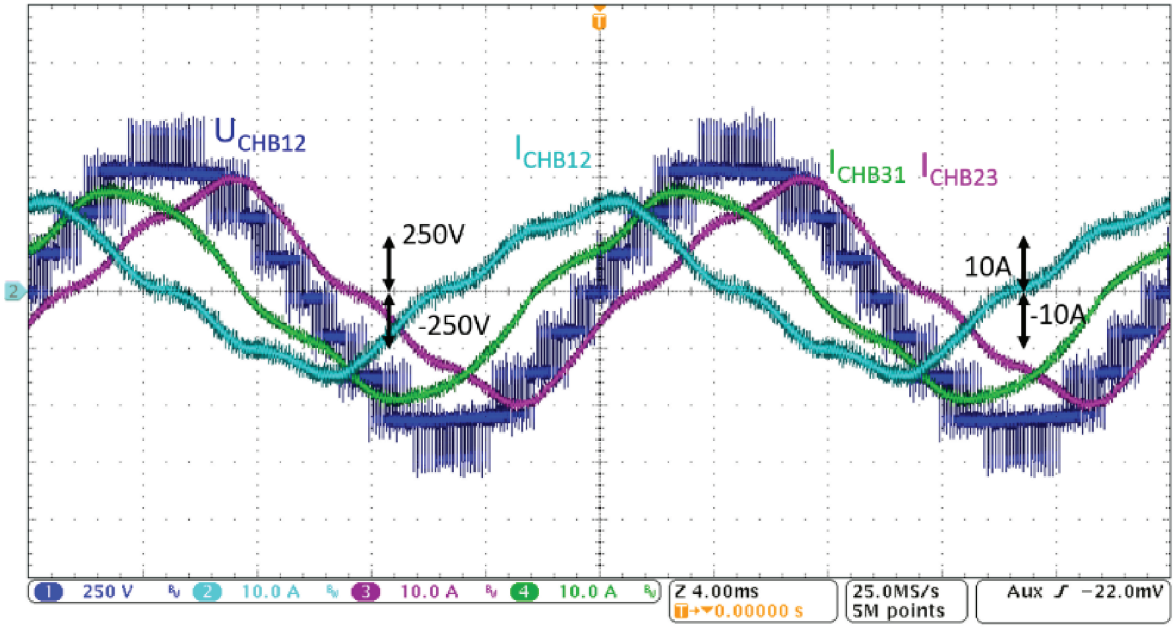

Figure 11. RL load, ARB—balancing ON + harmonics filtration OFF, blue U_{CHB12} [250 V/div], cyan I_{CHB12} [10 A/div], purple I_{CHB23} [10 A/div], green I_{CHB31} [10 A/div]. ARB, advanced rail balancer.

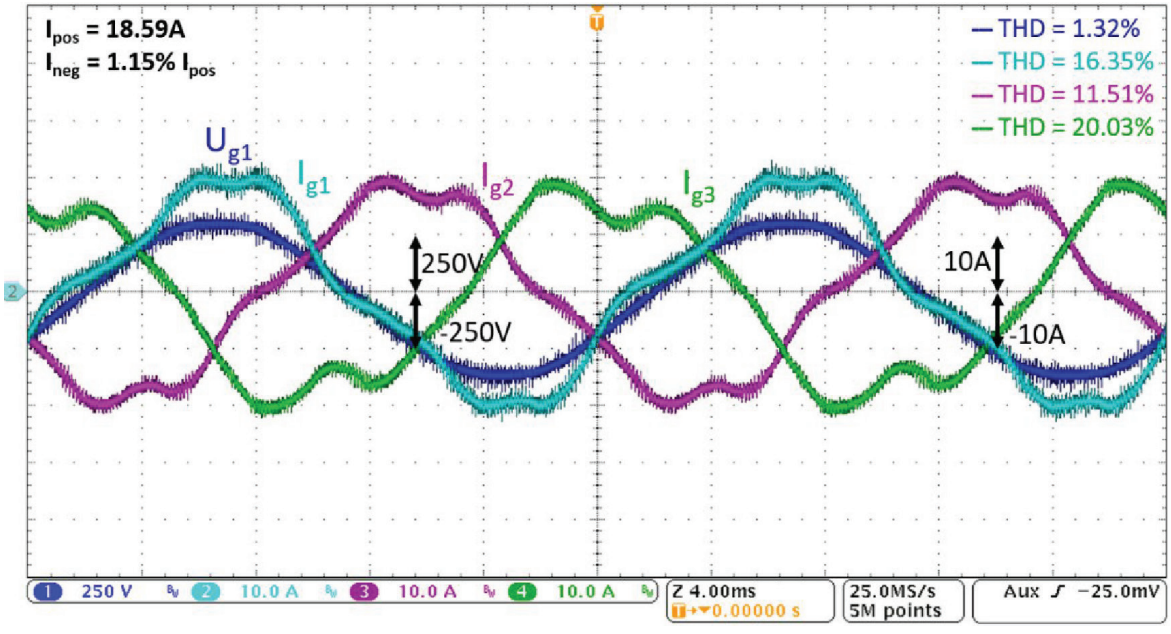

Figure 12. RL load, ARB—balancing ON + harmonics filtration OFF, blue U_{g1} [250 V/div], cyan I_{g1} [10 A/div], purple I_{g2} [10 A/div], green I_{g3} [10 A/div]. ARB, advanced rail balancer; THD, total harmonic distortion.

- Active filtering of higher-order (non-fundamental) current harmonics.
- Elimination of the resonant frequency shifts typically introduced by discretisation and large sampling times.
- Compensation of latency in the control/resonant system caused by sampling and modulation.

The proposed phase-by-phase current control algorithm employs a new resonant controller design derived from an analytical solution of exact discretisation, which inherently preserves the desired resonant frequency. This structure enables direct latency compensation and low computational burden, making it more suitable for

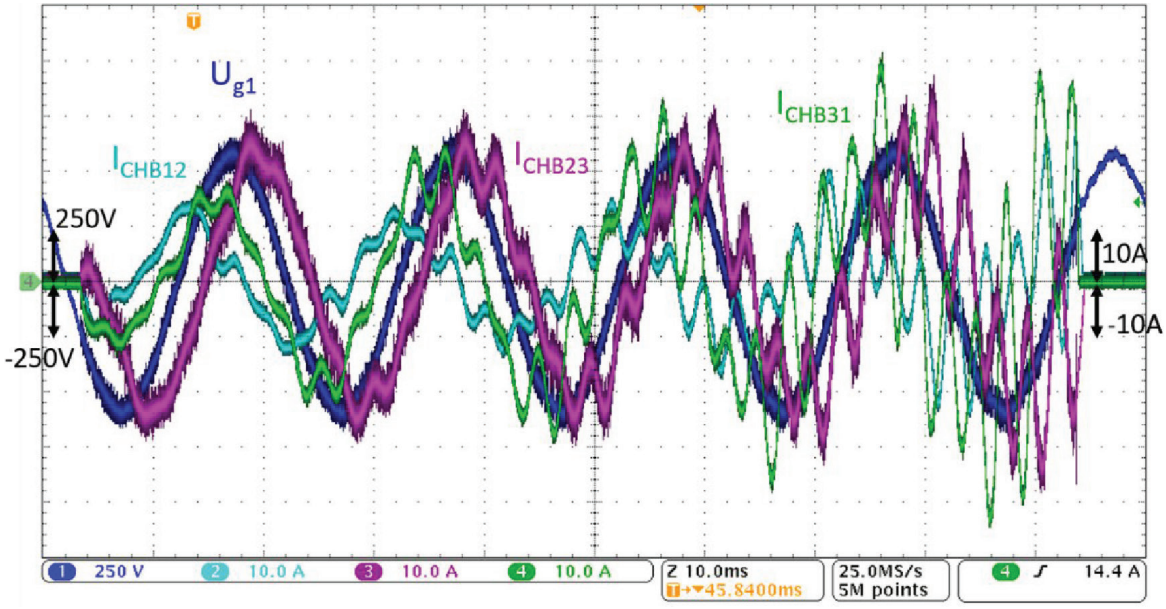

Figure 13. RL load, ARB—balancing ON + harmonics filtration ON, common R controllers, blue U_{g1} [250 V/div], cyan I_{CHB12} [10 A/div], purple I_{CHB23} [10 A/div], green I_{CHB31} [10 A/div]. ARB, advanced rail balancer.

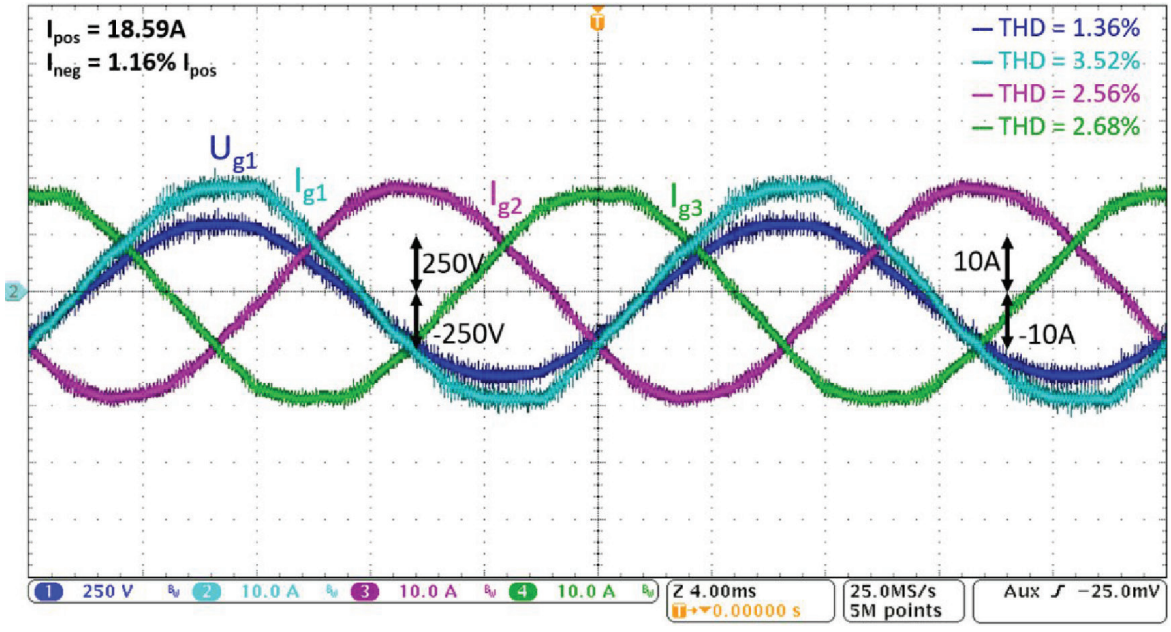

Figure 14. RL load, ARB—balancing ON + harmonics filtration ON, advanced R controllers, blue U_{g1} [250 V/div], cyan I_{g1} [10 A/div], purple I_{g2} [10 A/div], green I_{g3} [10 A/div]. ARB, advanced rail balancer; THD, total harmonic distortion.

low switching frequency applications. Additionally, the orthogonal structure of the controller's output signals allows simple extension with sinusoidal saturation (anti-windup) protection or using results for feedforward calculations.

Experimental results confirm the efficiency of the proposed controller, demonstrating great performance in high-order harmonics filtration, even with a significant control delay. Compared to a traditional implementation, the proposed algorithm demonstrates great accuracy and robustness, confirming its suitability for a wide range of practical applications.

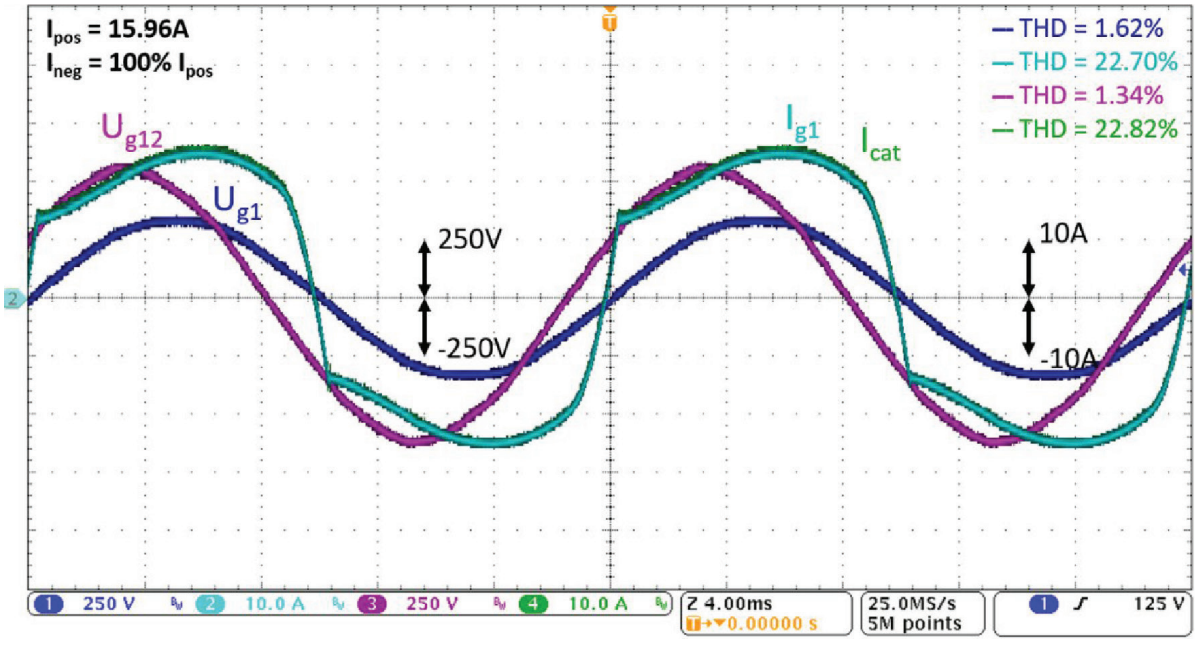

Figure 15. Load: Diode rectifier with RL load, ARB off, blue U_{g1} [250 V/div], cyan I_{g1} [10 A/div], purple U_{g12} [250 V/div], green I_{cat} [10 A/div] (aligned with I_{g1}). ARB, advanced rail balancer; THD, total harmonic distortion.

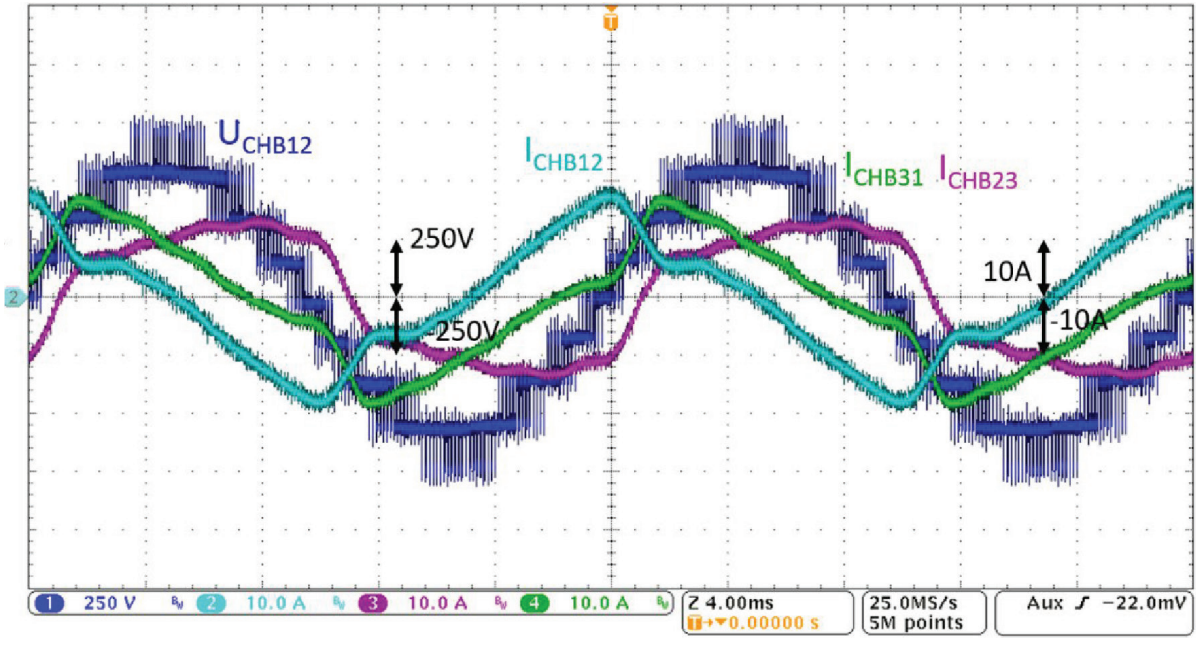

Figure 16. Load: Diode rectifier with RL load, ARB—balancing ON + harmonics filtration ON with advanced R controllers, blue U_{CHB12} [250 V/div], cyan I_{CHB12} [10 A/div], purple I_{CHB23} [10 A/div], green I_{CHB31} [10 A/div]. ARB, advanced rail balancer.

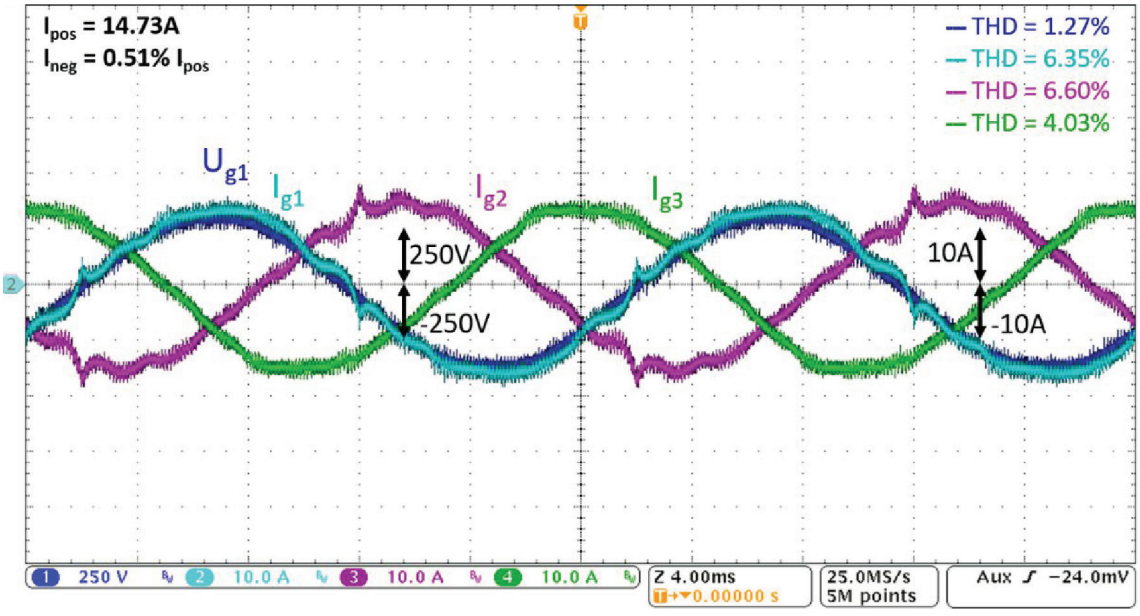

Figure 17. Load: Diode rectifier with RL load, ARB—balancing ON + harmonics filtration ON with advanced R controllers, blue U_{g1} [250 V/div], cyan I_{g1} [10 A/div], purple I_{g2} [10 A/div], green I_{g3} [10 A/div]. ARB, advanced rail balancer; THD, total harmonic distortion.

Acknowledgements

This research has been supported by the Ministry of Education, Youth and Sports of the Czech Republic under project SGS-2024-017.

References

Abdel-Aziz, A. A., Elgenedy, M. A. and Williams, B. W. (2024). Model Predictive Current Control for Low-Cost Shunt Active Power Filter. *CSEE Journal of Power and Energy Systems*, 10(4), pp. 1589–1598. doi: 10.17775/cseejpes.2023.00570

Aguilera, R. P., Acuna, P., Rojas, C., Pou, J., Konstantinou, G. and Watanabe, E. H. (2024). An Instantaneous Power Theory Extension for the Inter-Phase Power Imbalance Problem. *IEEE Transactions on Power Electronics*, 39(10), pp. 12261–12270. doi: 10.1109/tpel.2024.3397788

Alcaide, A. M., Leon, J. I., Portillo, R., Yin, J., Luo, W., Vazquez, S., Kouro, S. and Franquelo, L. G. (2021). Variable-Angle PS-PWM Technique for Multilevel Cascaded H-Bridge Converters with Large Number of Power Cells. *IEEE Transactions on Industrial Electronics*, 68(8), pp. 6773–6783. doi: 10.1109/tie.2020.3000121

Alonso Orcajo, G. A., Rodriguez Diez, J., Cano, J. M., Norniella, J. G., Pedrayes, G., Francisco, J., Rojas, C. H., Ardura, G. P. and Cifrián, R. D. (2020). Enhancement of Power Quality in an Actual Hot Rolling Mill Plant through a STATCOM. *IEEE Transactions on Industry Applications*, 56(3), pp. 3238–3249. doi: 10.1109/tia.2020.2976034

Biyya, I., Oubrahim, Z. and Abbou, A. (2023). PQ and DQ control methods against voltage disturbances for Shunt Active Power Filter – A Comparative Study. In: *2019 4th IEEE Workshop on the Electronic Grid (eGRID)*. [online] Karlsruhe, Germany: IEEE, pp.1–5. doi: 10.1109/egrid58358.2023.10380888.

Blahnik, V., Kosan, T., Peroutka, Z. and Talla, J. (2018). Control of a Single-Phase Cascaded H-Bridge Active Rectifier under Unbalanced Load. *IEEE Transactions on Power Electronics*, 33(6), pp. 5519–5527. doi: 10.1109/tpel.2017.2748218

Chai, M. (2018). Dual-Model Predictive Control for Cascaded H-Bridge Multilevel Active Rectifier with DC Voltage Balancing in a Solid-State Transformer. In: *2018 IEEE Energy Conversion Congress and Exposition (ECCE)*. [online] Energy Conversion Congress and Exposition (ECCE). IEEE, pp.1–7. Available at: https://ieeexplore.ieee.org/document/8557993 [Accessed 22 Sep. 2025].

Chavali, R. V., Dey, A. and Das, B. (2022). A Hysteresis Current Controller PWM Scheme Applied to Three-Level NPC Inverter for Distributed Generation Interface. *IEEE Transactions on Power Electronics*, 37(2), pp. 1486–1495. doi: 10.1109/tpel.2021.3107618

Deng, H., Fang, J., Qi, Y., Tang, Y. and Debusschere, V. (2023). A Generic Voltage Control for Grid-Forming Converters with Improved Power Loop Dynamics. *IEEE Transactions on Industrial Electronics*, 70(4), pp. 3933–3943. doi: 10.1109/tie.2022.3176308

Fei, J., Zhang, L., Zhuo, J. and Fang, Y. (2023). Wavelet Fuzzy Neural Supertwisting Sliding Mode Control of an Active Power Filter. *IEEE Transactions on Fuzzy Systems*, 31(11), pp. 4051–4063. doi: 10.1109/tfuzz.2023.3272028

Ferreira, S. C., Gonzatti, R. B., Pereira, R. R., da Silva, C. H., da Silva, L. E. B. and Lambert-Torres, G. (2018). Finite Control Set Model Predictive Control for Dynamic Reactive Power Compensation with Hybrid Active Power Filters. *IEEE Transactions on Industrial Electronics*, 65(3), pp. 2608–2617. doi: 10.1109/tie.2017.2740819

He, T., Wu, M., Aguilera, R. P., Lu, D. D. C., Liu, Q. and Vazquez, S. (2023). Low Computational Burden Model Predictive Control for Single-Phase Cascaded H-Bridge Converters without Weighting Factor. *IEEE Transactions on Industrial Electronics*, 70(3), pp. 2396–2406. doi: 10.1109/tie.2022.3167133

He, X., Geng, H. and Yang, G. (2018). A Generalized Design Framework of Notch Filter Based Frequency-Locked Loop for Three-Phase Grid Voltage. *IEEE Transactions on Industrial Electronics*, 65(9), pp. 7072–7084. doi: 10.1109/tie.2017.2784413

Husev, O., Roncero-Clemente, C., Makovenko, E., Pimentel, S. P., Vinnikov, D. and Martins, J. (2020). Optimization and Implementation of the Proportional-Resonant Controller for Grid-Connected Inverter with Significant Computation Delay. *IEEE Transactions on Industrial Electronics*, 67(2), pp. 1201–1211. doi: 10.1109/tie.2019.2898616

Khan, S. A., Guo, Y., Siwakoti, Y. P., Lu, D. D. C. and Zhu, J. (2020). A Disturbance Rejection-Based Control Strategy for Five-Level T-Type Hybrid Power Converters with Ripple Voltage Estimation Capability. *IEEE Transactions on Industrial Electronics*, 67(9), pp. 7364–7374. doi: 10.1109/tie.2019.2942550

Lamb, J., Mirafzal, B. and Blaabjerg, F. (2018). PWM Common Mode Reference Generation for Maximizing the Linear Modulation Region of CHB Converters in Islanded Microgrids. *IEEE Transactions on Industrial Electronics*, 65(7), pp. 5250–5259. doi: 10.1109/tie.2017.2777401

Lezana, P., Silva, C. A., Rodríguez, J. and Pérez, M. A. (2007). Zero-Steady-State-Error Input-Current Controller for Regenerative Multilevel Converters Based on Single-Phase Cells. *IEEE Transactions on Industrial Electronics*, 54(2), pp. 733–740. doi: 10.1109/tie.2007.891994

Marquez, A., Leon, J. I., Monopoli, V. G., Vazquez, S., Liserre, M. and Franquelo, L. G. (2020). Generalized Harmonic Control for CHB Converters with Unbalanced Cells Operation. *IEEE Transactions on Industrial Electronics*, 67(11), pp. 9039–9047. doi: 10.1109/tie.2019.2956383

Ma, J., Wang, X., Blaabjerg, F., Song, W., Wang, S. and Liu, T. (2020). Multisampling Method for Single-Phase Grid-Connected Cascaded H-Bridge Inverters. *IEEE Transactions on Industrial Electronics*, 67(10), pp. 8322–8334. doi: 10.1109/tie.2019.2947864

Moradi, A. and Pichan, M. (2022). A High Performance Harmonic Detection Method Based on Wavelet Transform for Shunt Active Power Filter with Experimental Verification. In: *2022 13th Power Electronics, Drive Systems, and Technologies Conference (PEDSTC)*. [online] Power Electronics, Drive Systems, and Technologies Conference (PEDSTC). IEEE. Available at: https://ieeexplore.ieee.org/document/9767253 [Accessed 22 Sep. 2025].

Nasiri, M. R., Farhangi, S. and Rodriguez, J. (2019). Model Predictive Control of a Multilevel CHB STATCOM in Wind Farm Application Using Diophantine Equations. *IEEE Transactions on Industrial Electronics*, 66(2), pp. 1213–1223. doi: 10.1109/tie.2018.2833055

Ouchen, S., Benbouzid, M., Blaabjerg, F., Betka, A. and Steinhart, H. (2021). Direct Power Control of Shunt Active Power Filter Using Space Vector Modulation Based on Supertwisting Sliding Mode Control. *IEEE Journal of Emerging and Selected Topics in Power Electronics*, 9(3), pp. 3243–3253. doi: 10.1109/jestpe.2020.3007900

Park, C. S. (2017). Guaranteed-Stable Sliding DFT Algorithm with Minimal Computational Requirements. *IEEE Transactions on Signal Processing*, 65(20), pp. 5281–5288. doi: 10.1109/tsp.2017.2726988

Pastor, M. and Dudrik, J. (2015). Predictive Control of Grid-Connected Multilevel Inverter with Output LCL Filter. *Elektronika ir Elektrotechnika*, 21(3), pp. 10–15. doi: 10.5755/j01.eee.21.3.10033

Santiprapan, P., Areerak, K. and Areerak, K. (2024). An Adaptive Gain of Proportional-Resonant Controller for an Active Power Filter. *IEEE Transactions on Power Electronics*, 39(1), pp. 1433–1446. doi: 10.1109/tpel.2023.3319476

Steimel, A. (2014). Electric Traction – Motive Power and Energy Supply: Basics and Practical Experience. 2nd en München: Div Deutscher Industrieverlag Gmbh, p. 412

Straka, M., Blahnik, V. and Pittermann, M. (2021). Comparison of Traction Substation Topologies for AC 25kV Electrical Railway. In: *IECON 2021 – 47th Annual Conference of the IEEE Industrial Electronics Society*. [online] IECON 2021 – 47th Annual Conference of the IEEE Industrial Electronics Society. IEEE, pp.1–6. doi: 10.1109/iecon48115.2021.9589924.

Suul, J. A., Luna, A., Rodriguez, P. and Undeland, T. (2012). Voltage-Sensor-Less Synchronization to Unbalanced Grids by Frequency-Adaptive Virtual Flux Estimation. *IEEE Transactions on Industrial Electronics*, 59(7), pp. 2910–2923. doi: 10.1109/TIE.2011.2168793

Tafti, H. D., Maswood, A. I., Konstantinou, G., Townsend, C. D., Acuna, P. and Pou, J. (2018). Flexible Control of Photovoltaic Grid-Connected Cascaded H-Bridge Converters During Unbalanced Voltage Sags. *IEEE Transactions on Industrial Electronics*, 65(8), pp. 6229–6238. doi: 10.1109/tie.2017.2786204

Talla, J. and Blahnik, V. (2017). Sliding DFT based grid to ground admittance estimation with guaranteed numerical stability. In: *IECON 2017 - 43rd Annual Conference of the IEEE Industrial Electronics Society.* [online] IECON 2017 - 43rd Annual Conference of the IEEE Industrial Electronics Society. pp.4344–4349. doi: 10.1109/iecon.2017.8216747.

Wang, H. and Liu, S. (2019). Harmonic Interaction Analysis of Delta-Connected Cascaded H-Bridge-Based Shunt Active Power Filter. *IEEE Journal of Emerging and Selected Topics in Power Electronics*, 8(3), pp. 2445–2460. doi: 10.1109/jestpe.2019.2930033

Wang, K., Zhu, R., Wei, C., Liu, F., Wu, X. and Liserre, M. (2019). Cascaded Multilevel Converter Topology for Large-Scale Photovoltaic System with Balanced Operation. *IEEE Transactions on Industrial Electronics*, 66(10), pp. 7694–7705. doi: 10.1109/TIE.2018.2885739

Wang, M., Zhang, X., Zhao, T., Ma, M., Hu, Y., Wang, F. and Wang, X. (2020). Harmonic Compensation Strategy for Single-Phase Cascaded H-Bridge PV Inverter under Unbalanced Power Conditions. *IEEE Transactions on Industrial Electronics*, 67(12), pp. 10474–10484. doi: 10.1109/tie.2019.2962461

Yepes, A. G., Freijedo, F. D., Doval-Gandoy, J., López, Ó, Malvar, J. and Fernandez-Comesaña, P. (2010). Effects of Discretization Methods on the Performance of Resonant Controllers. *IEEE Transactions on Power Electronics*, 25(7), pp. 1692–1712. doi: 10.1109/tpel.2010.2041256

Yu, Y., Konstantinou, G., Townsend, C. D., Aguilera, R. P. and Agelidis, V. G. (2017). Delta-Connected Cascaded H-Bridge Multilevel Converters for Large-Scale Photovoltaic Grid Integration. *IEEE Transactions on Industrial Electronics*, 64(11), pp. 8877–8886. doi: 10.1109/tie.2016.2645885

Zhang, Y., Yuan, X., Wu, X., Yuan, Y. and Zhou, J. (2020). Parallel Implementation of Model Predictive Control for Multilevel Cascaded H-Bridge STATCOM with Linear Complexity. *IEEE Transactions on Industrial Electronics*, 67(2), pp. 832–841. doi: 10.1109/tie.2019.2901647

Zhao, T. and Chen, D. (2022). A Power Adaptive Control Strategy for Further Extending the Operation Range of Single-Phase Cascaded H-Bridge Multilevel PV Inverter. *IEEE Transactions on Industrial Electronics*, 69(2), pp. 1509–1520. doi: 10.1109/TIE.2021.3060646